Research

Author for correspondence:
Leo H. O. Hellström
e-mail: lhellstr@princeton.edu

Structure identification in pipe flow using proper orthogonal decomposition

Leo H. O. Hellström and Alexander J. Smits

Mechanical and Aerospace Engineering, Princeton University, Princeton, NJ 08544, USA

LHO, 0000-0002-1773-8875; AJS, 0000-0002-3883-8648

The energetic motions in direct numerical simulations of turbulent pipe flow at $Re_\tau = 685$ are investigated using proper orthogonal decomposition. The procedure is extended such that a pressure component is identified in addition to the three-component velocity field for each mode. The pressure component of the modes is shown to align with the streamwise velocity component associated with the large-scale motions, where positive pressure coincides with positive streamwise velocity, and vice versa. The streamwise evolution of structures is then visualized using a conditional mode, which exhibit a strong similarity to the large-scale, low-momentum motions. A low-pressure region is present in the downstream section of the structure, and a high-pressure region is present in the upstream section.

This article is part of the themed issue 'Toward the development of high-fidelity models of wall turbulence at large Reynolds number'.

1. Introduction

The structure of the organized motions in turbulent wall-bounded flows has been investigated in a wide variety of ways that include temporal and spatial correlations of the velocity field [1–3], flow visualizations of passive scalar fields [4–7], and, more recently, constructions of the three-dimensional velocity or vorticity fields derived using numerical or experimental data [8–11]. Here, we will discuss the advantages of using proper orthogonal decomposition (POD) to gain further insight in the structure of turbulence in pipe flow over a wide range of Reynolds numbers.

THE ROYAL SOCIETY PUBLISHING

POD, also known as principal component analysis, the Karhunen–Loève decomposition, or singular value decomposition, may be used to construct a low-dimensional description of turbulence that captures the most energetic contributions to the turbulence kinetic energy [12]. That is, POD is used to extract a set of basis functions for a modal decomposition from an ensemble of signals. It creates a mathematical model of the flow that decouples the spatial structures from its temporal behaviour. The principal steps are described in more detail in §2, but the general approach is to start with a numerical or experimental dataset on the fluctuating velocity field, where the eigenfunctions of the cross-correlation tensor are the spatial POD modes and the corresponding eigenvalues represent their contribution to the energy. The temporal evolution of the modes can be described by the POD coefficients which are acquired by projecting each mode back onto the fluctuating velocity field. The modes are generally ranked in terms of their energy content, and typically only a reduced set of the most energetic modes are retained as representations of the underlying flow structure.

Early attempts to use POD on experimental data in pipe flow were limited to the near wall region, and proved to be difficult to implement because the two-point measurements needed to construct the correlation matrix required a very time-consuming effort [13,14]. Despite the experimental challenges, POD was successful in identifying the near-wall structures as pairs of counter-rotating streamwise vortices [15]. DNS studies of turbulent channel flows proved to be more amenable to POD analysis, and the results showed that the dominant statistical structure in the near-wall region was a roll-like motion [16]. For these low Reynolds numbers flows ($Re_\tau = u_\tau \delta / \nu = 80$–$180$), the first 25 modes captured 70% of the energy [16–18]. Here, ν is the fluid kinematic viscosity, u_τ is the friction velocity and δ is the characteristic outer length scale.

Further progress in investigating the organized motions was closely linked to the development of high-resolution particle image velocimetry (PIV), especially stereoscopic PIV [19,20], and to higher Reynolds number numerical simulations [21]. These approaches yield velocities at all spatial points simultaneously, which is beneficial when constructing the two-point correlation tensor for POD, and yielded a detailed statistical picture of the spatially coherent structures [9]. The POD method was made even more accessible by the introduction of snapshot POD [22]. In snapshot POD, it is assumed that the flow field is separable into a spatial and a temporal function, which reduces the dimension of the cross-correlation tensor from ($N_x \times N_x$) to ($N_t \times N_t$), where N_x and N_t represents the number of spatial and temporal points, respectively. The question of whether the flow is separable in time and space is not yet fully answered, and differences in the results obtained using the two methods have been observed [23].

In general, it seems that the POD approach is well suited to the study of organized or coherent motions in turbulent flows. For turbulent wall-bounded flows, the coherent motions may be classified into four distinct groups [24]. The first group is identified as the near-wall streaks, which are streamwise streaks of low-momentum fluid. These streaks are located in the viscous sublayer with a typical spanwise spacing of $100\nu/u_\tau$ and were identified as roll-like motions by near-wall POD analyses [15]. The second group is the loop-like horseshoe or hairpin-vortices, which span a wide range of scales with a minimum height of about $100\nu/u_\tau$. The hairpin-vortex induces a low-momentum region between its legs, while carrying a low-pressure signature upstream of its front and a high-pressure region downstream of its back [9,25]. The hairpin-vortices are believed to align into larger groups of $\mathcal{O}(2-3\delta)$ motions travelling at a common convective velocity, creating the third group of coherent structures, often referred to as hairpin packets or large-scale motions (LSMs) [9]. The last group encompasses the largest known coherent structures, known as the very-large-scale motions (VLSMs) in pipe flow, and superstructures in boundary layer flows. The VLSM is characterized by a long meandering region of low momentum fluid with a streamwise extent $\mathcal{O}(7\delta)$, although they may occasionally extend as far as 30δ [3,26]. The origin of the VLSMs is still uncertain but is believed to be a caused by a pseudo-streamwise alignment of LSMs [3,27], although the underlying mechanism for such alignment is still unknown.

When the flow geometry displays some symmetries, as in pipe flow, the POD modes in any periodic (or homogeneous) direction are reduced to a Fourier series (or Fourier transform). These modes are known in advance, and such decompositions accelerate the POD modal
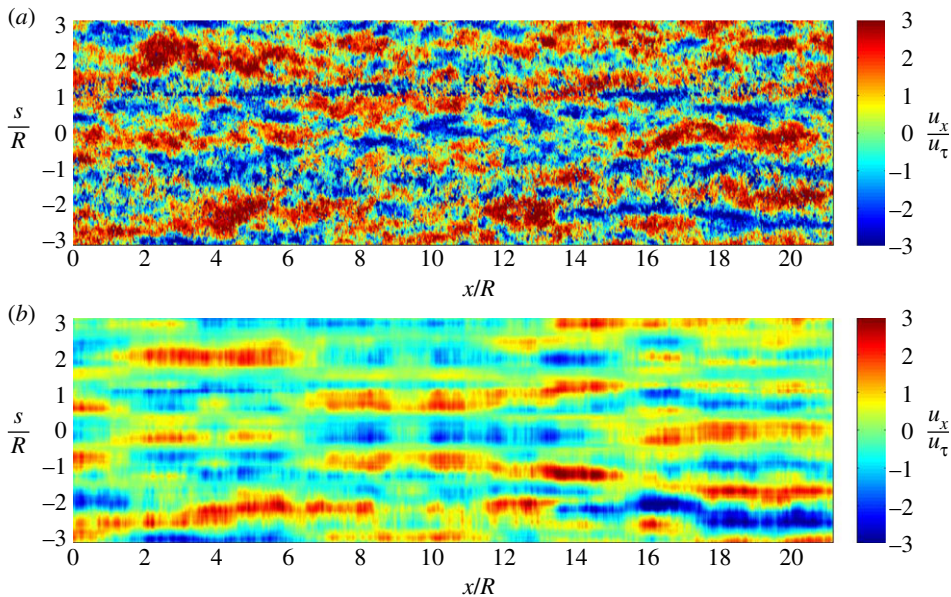
Figure 1. Carpet plots constructed using Taylor's hypothesis showing the streamwise velocity fluctuations at wall-normal distance of $y/R = 0.2$ and $Re_D = 12\,500$, taken from [28]. (a) instantaneous streamwise fluctuations (b) the first four POD modes reconstructed and superimposed. Flow is from left to right.

convergence [23]. Hence, turbulent pipe flow is well suited to POD, and it has been the focus of a number of previous studies.

Early experimental studies of POD in pipe flow focused on the near-wall region to model the near-wall cycle of turbulence [13,15]. These studies were extended by Hellström *et al.* [28], who performed a POD analysis on time-resolved stereo PIV data in the cross-stream plane of pipe flow at $Re_D = U_b 2R/\nu = 12\,500$, thereby revealing the structure of the LSMs and VLSMs. Here, U_b is the bulk velocity and R is the pipe radius. Figure 1a displays some results on the instantaneous streamwise velocity fluctuations u_x/u_τ at a wall distance $y/R = 0.2$ using Taylor's hypothesis. The reconstructed flow field using the first four POD modes is shown in figure 1b, and it can be seen that the large-scale features of the flow, particularly the VLSM, can be reconstructed using a small number of the most energetic POD modes. These structures were found to extend far into the wake region.

Hellström & Smits [23] performed a similar analysis at a higher Reynolds number (Re_D of 100 000), and showed that the dominant motions consisted of three azimuthal and one radial structure, where the azimuthal mode number (m) defines its azimuthal length scale. These POD structures bear close resemblance to those found by Bailey & Smits [29] at a similar Reynolds number using two-point correlation techniques to identify the most energetic structure.

Baltzer *et al.* [30] performed a direct numerical simulation of turbulent pipe flow at $Re_D = 24\,580$ and found the lower order modes to be roll-cell like structures, and related these structures to the LSMs which lined up to create the VLSMs with a streamwise length of 15–30R. Hellström *et al.* [27] conducted an experiment with a dual-plane PIV set-up and showed that the azimuthally decomposed POD modes describe the LSMs with a spanwise length defined by the azimuthal mode number, and that the radial evolution of the LSM was described by a transition between POD modes. Figure 2 shows a set of these modes that together represent an LSM, using the fifth azimuthal mode and POD modes one to three [31]. It can also be seen that these modes define roll-like motions with a negative correlation between the streamwise and wall-normal components, so that these structures directly contribute to the Reynolds shear stress ($-\overline{uv} > 0$).
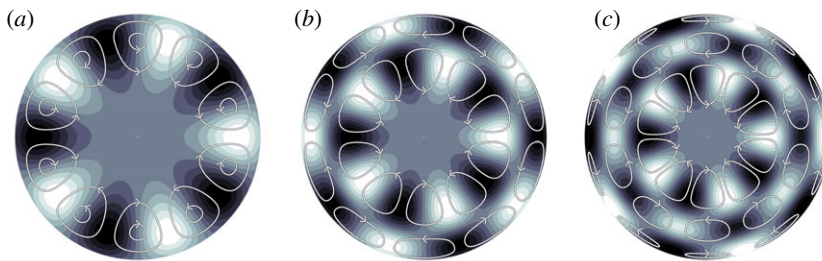
4

rsta.royalsocietypublishing.org *Phil. Trans. R. Soc. A* **375**: 20160086

Figure 2. Contour plots of the streamwise component of the POD modes for $Re_D = 104\,000$, white and black represent positive and negative values, respectively. Streamlines indicate the in-plane component of the modes. (*a*) first POD mode, (*b*) second POD mode and (*c*) third POD mode. All modes are shown with azimuthal mode five. Taken from Hellström *et al.* [31]. (Online version in colour.)
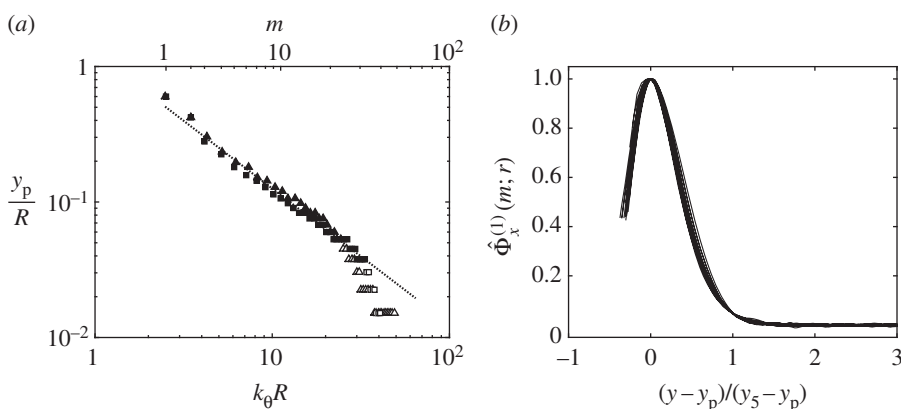

Figure 3. (*a*) The peak locations for the first POD mode and azimuthal mode numbers $m \in [1, 64]$ filled triangles, $Re_D = 51\,700$; filled squares, $Re_D = 104\,000$; dotted lines, $y_p/R = 2\pi C\,(k_\theta R)^{-1}$, with $C = 0.2$. Modes with a peak location $y_p^+ < 75$ are identified with open symbols. The lower abscissa indicates the azimuthal wavenumber, while the upper abscissa shows the corresponding azimuthal mode number, for $Re_D = 104\,000$. (*b*) The non-dimensionalized POD modes for $m \in [5, 40]$. The modes are scaled using the wall-normal distance from its peak to where it reaches 5% of its peak value, due to limitations of estimating the wall normal location. Taken from Hellström *et al.* [31].

Hellström *et al.* [27] further concluded that the LSM can line up to create the VLSMs. In addition, these structures were later shown to be insensitive to Reynolds number, and that they had a similar shape and behaviour in the slug section of a transitional pipe flow as in a fully turbulent pipe flow [32].

In related work, Hwang [33] showed that the most energetic structures in a channel flow are the self-similar structures in the log-layer, and suggested that the size of each of these structures is characterized by its spanwise length scale. Similarly, Hellström *et al.* [31] showed that the azimuthally decomposed POD modes are in fact self-similar with respect to its azimuthal mode number. This was identified by tracking the wall-normal peak location (y_p) for the first POD mode with respect to its azimuthal wavenumber k_θ. This relationship is shown in figure 3*a*, where the peak location follows the self-similar behaviour $y_p/R = 2\pi C(k_\theta R)^{-1}$, shown by the dotted line. By using this scaling, it was then shown that the radial profile of the modes could be collapsed on to a representative profile, as displayed in figure 3*b*.

We now build on this previous work to examine the DNS data of Wu *et al.* [34] at $Re_D = 24\,580$ ($Re_\tau = 685$). In particular, we are interested in the pressure field, something that is extremely difficult to obtain in any experimental study, and its relationship to the velocity field.

2. Proper orthogonal decomposition

Here, we use 600 DNS data blocks for $Re_D = 24\,580$, acquired by Wu *et al.* [34], where each block domain is $30R$ long with a grid resolution $[r, \theta, x] = [256, 1024, 2048]$, with a streamwise periodic boundary condition. The blocks are acquired every $100\,\Delta t$, corresponding to a convective bulk flow displacement of $0.9R$. Additional details of the simulation are given by Wu & Moin [10].

Along with performing POD, we will also introduce a procedure to extract a mode representing a scalar field, specifically the fluctuating pressure field. In contrast to the velocity field, the pressure field in an incompressible flow is a global quantity and any point in the flow will simultaneously affect all other points. To that end, the POD procedure needs to be simultaneously solved for the complete flow field, and cannot be approached using sliced POD. We begin, however, by following the procedure of Hellström *et al.* [27], using a snapshot POD analysis of the three-component fluctuating velocity data. The flow is considered periodic both in the azimuthal and streamwise directions and can, due to the translation and rotation symmetries, be decomposed into azimuthal (m) and streamwise mode numbers (k).

We start with the 'direct' POD equation, where the cross-correlation tensor depends on the azimuthal mode number, streamwise wavenumber and the radial two-point correlation represented by r and r'. The eigenvalue problem becomes

$$\int_{r'} \mathbf{S}(k; m; r, r') \Phi^{(n)}(k; m; r') r' \, \mathrm{d}r' = \lambda^{(n)}(k; m) \Phi^{(n)}(k; m; r), \tag{2.1}$$

where n represents the POD mode number, $\Phi^{(n)}$ are the radial eigenfunctions with the corresponding eigenvalues $\lambda^{(n)}$, and there exist a set of (n) radial modes for each azimuthal and streamwise mode number combination. The time-averaged cross-correlation tensor, $\mathbf{S}$, is defined as

$$\mathbf{S}(k; m; r, r') = \lim_{\tau \to \infty} \frac{1}{\tau} \int_0^\tau \mathbf{u}(k; m; r, t) \mathbf{u}^*(k; m; r', t) \, \mathrm{d}t, \tag{2.2}$$

where $\mathbf{u}$ represents the three-component velocity field, and $*$ is its conjugate transpose. The method of snapshots assumes that the flow is separable in time and space, which can be written as

$$\alpha^{(n)}(k; m; t) = \int_r \mathbf{u}(k; m; r, t) \Phi^{(n)*}(k; m; r) r \, \mathrm{d}r. \tag{2.3}$$

The eigenvalue problem can now be rewritten to identify the POD coefficients $\alpha^{(n)}$,

$$\lim_{\tau \to \infty} \frac{1}{\tau} \int_0^\tau \mathbf{R}(k; m; t, t') \alpha^{(n)}(k; m; t') \, \mathrm{d}t' = \lambda^{(n)}(k; m) \alpha^{(n)}(k; m; t). \tag{2.4}$$

The cross-correlation tensor $\mathbf{R}$ is defined as $\mathbf{R}(k; m; t, t') = \int_r \mathbf{u}(k; m; r, t) \mathbf{u}^*(k; m; r, t') r \, \mathrm{d}r$. This tensor is now transformed from $[3r \times 3r']$ to a $[t \times t']$ tensor, which represents a 40% reduction in computational effort. However, the more significant benefit lies in the construction of the modes

$$\lim_{\tau \to \infty} \frac{1}{\tau} \int_0^\tau \mathbf{u}_\mathrm{T}(k; m; r, t) \alpha^{(n)*}(k; m; t) \, \mathrm{d}t = \Phi_\mathrm{T}^{(n)}(k; m; r) \lambda^{(n)}(k; m). \tag{2.5}$$

We are now free to choose $\mathbf{u}_\mathrm{T}$ to represent the total fluctuation field, such as the velocity or any scalar quantity we wish to represent in modal form. As long as $\mathbf{u}$ in equation (2.2) is the three component fluctuating velocity, the modes will be sorted by their energy content, represented by $\lambda^{(n)}$. Here, $\mathbf{u}_\mathrm{T}$ will represent the fluctuating three component velocity and pressure fields, $[u_x, u_r, u_\theta, p]^\mathrm{T}$ and also $\Phi_\mathrm{T}^{(n)} = [\Phi_x^{(n)}, \Phi_r^{(n)}, \Phi_\theta^{(n)}, \Phi_\mathrm{P}^{(n)}]^\mathrm{T}$. The POD modes obey conjugate and

reflection symmetries in the (r, θ)-plane, and can be expressed as

$$\Phi_x^{(n)}(k; m; r) = \Phi_x^{(n)}(k; -m; r) = \Phi_x^{(n)*}(-k; m; r),$$

$$\Phi_r^{(n)}(k; m; r) = \Phi_r^{(n)}(k; -m; r) = \Phi_r^{(n)*}(-k; m; r),$$

$$\Phi_\theta^{(n)}(k; m; r) = -\Phi_\theta^{(n)}(k; -m; r) = -\Phi_\theta^{(n)*}(-k; m; r)$$

and

$$\Phi_{\rm P}^{(n)}(k; m; r) = \Phi_{\rm P}^{(n)}(k; -m; r) = \Phi_{\rm P}^{(n)*}(-k; m; r).$$

From here on, therefore, we only consider modes with positive m, and modes with $\pm k$ are taken to be conjugate pairs which together compose the turbulent structures [35].

To visualize the streamwise evolution of the structures represented by the POD modes, we also create a conditional mode $\Psi^{(n)}(m; \xi, r)$. We create the mode by performing an inner product between the inverse Fourier transformed POD coefficients ($\alpha^{(n)}(m; x, t)$) and the azimuthally Fourier transformed flow field. That is,

$$\Psi^{(n)}(m; \xi, r) := \lim_{\chi \to \infty} \frac{1}{\chi} \int_0^\chi \lim_{\tau \to \infty} \frac{1}{\tau} \int_0^\tau \mathbf{u}_{\rm T}(m; r, x + \xi, t) \alpha^{(n)}(m; x, t) \, {\rm d}t \, {\rm d}x. \tag{2.6}$$

This procedure generates a conditional structure where the condition is applied at $\xi = 0$, and where the upstream and downstream structure is allowed to evolve without any radial restrictions. In fact, at $\xi = 0$ the cross-sectional profile of the conditional mode becomes the snapshot POD modes.

3. Discussion

The POD modes are insensitive to the streamwise mode number, and we will therefore present the energy as integrated over all k. The POD analysis is truncated due to the large amount of data and is resolved up to $[\pm k, m, n] = [2 \times 128, 64, 256]$, corresponding to azimuthal and streamwise wavelengths $\lambda_\theta/R = 0.098$ and $\lambda_x/R = 0.234$. These resolved modes capture 95.4% of the total turbulent kinetic energy. The relative kinetic energies for each of the first five POD modes and first 20 azimuthal modes are shown in figure 4.

As found by Hellström *et al.* [27], the most energetic modes each contain about 4–5% of the total energy, with mode $(n, m) = (1, 3)$ being the most energetic, followed by azimuthal modes two and four. Furthermore, the integrated energy for the first POD mode and the first 20 azimuthal modes represents approximately 37% of the total energy, and 61% when considering the first five POD modes. The corresponding values for $Re_D = 104\,000$ were 25% and 45%, respectively, indicating that at lower Reynolds number the flow may be represented by fewer modes.

As a part of the POD analysis, each mode has been normalized such that its l^2-norm is unity. As indicated earlier, the modes are highly insensitive to streamwise wavenumber, and so they will be presented as an average over k, which due to the conjugate symmetries is real and indicated as $\langle \cdot \rangle_k$. The streamwise velocity component of the first and second POD modes, $\langle \Phi_x^{(n)}(k; m; r) \rangle_k$, with azimuthal mode numbers $m \in \{5, 10, 15, 20, 25, 30, 35, 40, 45, 50\}$, are shown in figure 5a, b. The wall-normal extent of the modes decreases as the azimuthal length scale decreases (or m increases). The pressure component of the averaged modes, $\langle \Phi_{\rm P}^{(n)}(k; m; r) \rangle_k$, are in phase with the streamwise velocity component of the modes, and are shown in figure 5c, d. The pressure modes shown in figure 5c share many similarities with the velocity modes; for example, their peak locations approach the wall with increasing azimuthal mode number. One significant difference, however, is that although the pressure modes decay when approaching the wall, as do the velocity modes, they do not go to zero because they do not need to obey the no-slip condition.

For clarity, a subset of the modes in figure 5 are reconstructed as cross-sectional modes in figure 6, which highlight the relationship between the three velocity components and the pressure component of the modes. Figure 6a, b shows the velocity components of the first radial modes for azimuthal mode numbers $m \in \{5, 10\}$. The streamwise component is shown using contours, where red and blue represent positive and negative values, respectively. The in-plane
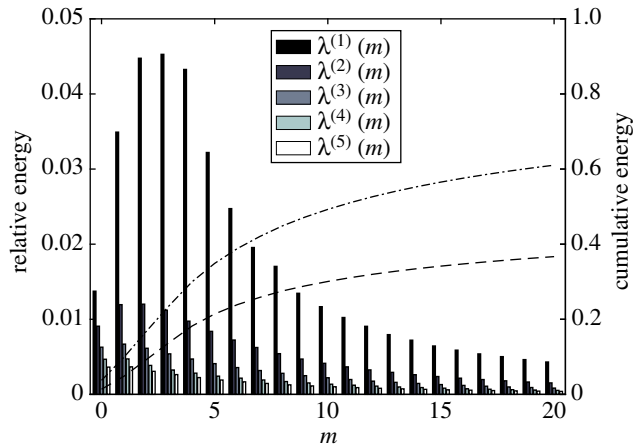
7

rsta.royalsocietypublishing.org   *Phil. Trans. R. Soc. A* **375**: 20160086

Figure 4. The bars show relative mode energy for the first five POD modes n and first 15 azimuthal modes m, integrated over all streamwise mode numbers k. The dashed line represents the cumulative energy for the first POD mode and dot-dashed line is the cumulative energy for the first five POD mode. (Online version in colour.)
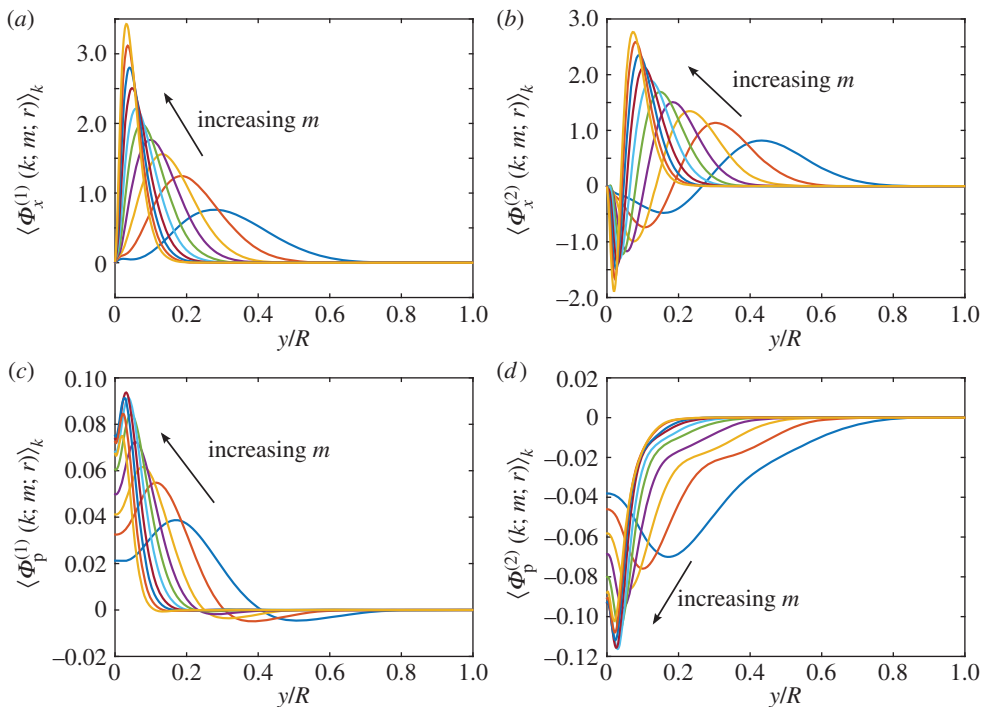

Figure 5. (a) Streamwise component of the first radial mode; (b) streamwise component of the second radial mode; (c) first pressure mode; and (d) second pressure mode. All figures are shown for azimuthal modes $m \in \{5, 10, 15, 20, 25, 30, 35, 40, 45, 50\}$. (Online version in colour.)

components of the modes are shown as streamlines and identifies a set of roll-like motions with a negative correlation between the streamwise and wall-normal components, making these structures positive contributors to the Reynolds shear stress $-\overline{uv}$ [23,27]. In figure 6c, d, we show the pressure component of the modes by contours, and the in-plane velocity components of the
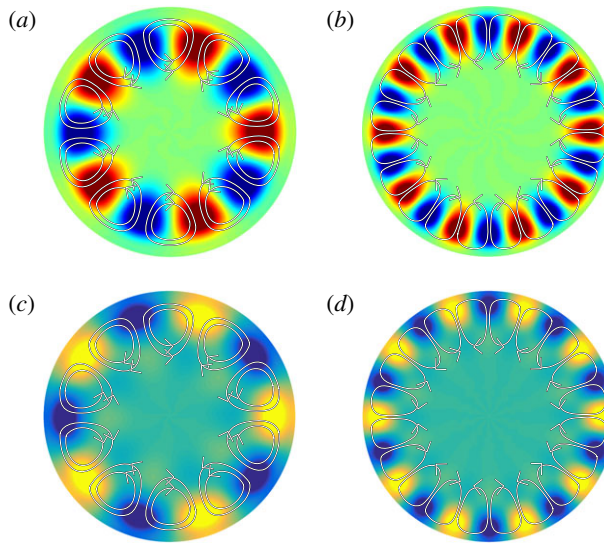
Figure 6. Reconstructed view of the first radial modes, $\langle \Phi_x^{(1)}(k;m;r) \rangle_k$ and $\langle \Phi_p^{(1)}(k;m;r) \rangle_k$. (*a*) Velocity mode for $m = 5$, (*b*) velocity mode for $m = 10$, (*c*) pressure mode for $m = 5$ and (*d*) pressure mode for $m = 10$. For velocity, red and blue represent positive and negative values, respectively, while for pressure yellow and blue represent positive and negative values, respectively.

modes are superposed on the pressure field to demonstrate their relationship to the velocity field. The pressure field is aligned with the streamwise velocity components, where the high- and low-pressure fluctuations are associated with the high and low streamwise momentum regions, respectively.

Hellström *et al.* [31] showed that the POD modes in pipe flow display self-similarity when scaled properly. Since the azimuthal direction is described by Fourier modes, which are inherently self-similar, only the radial direction needs to be considered for a complete similarity analysis in the pipe cross-section. Demonstrating that there exists a set of self-similar energetic structures may provide a possible link between the energetic structures suggested by Lumley and those providing the framework for Townsend's 'attached eddy' hypothesis. The attached eddy hypothesis prescribes eddies (or structures) to be self-similar in the absence of viscosity, where the structures are characterized by a length-scale proportionate to their distance to the wall. Hellström *et al.* [31] suggested that this length scale could be expressed as the wall-normal distance of the mode maximum of $\langle \Phi_x^{(1)} \rangle_k$, y_p.

Figure 7 shows the wall-normal peak location (y_p/R) of the first POD modes with respect to their azimuthal wavenumber $k_\theta R = 2\pi R/\lambda_\theta$, where $\lambda_\theta = 2\pi(R - y_\mathrm{p})/m$. In the case of a self-similar behaviour, the modes are expected to have a constant aspect ratio and follow $y_\mathrm{p}/R = 2\pi C(k_\theta R)^{-1}$, where C is a constant and here estimated to be 0.36. The same constant was estimated to be 0.2 by Hellström *et al.* [31], suggesting that the aspect ratio of the structure changes with Reynolds number. This observation, however, is consistent with previous findings where the peak location for a chosen m approached the wall with increasing Reynolds numbers [23]. For the current Reynolds number, there is a narrow range for which the mode peaks exhibit a self-similar behaviour ($8 \leq m \leq 18$), indicated by filled triangles in figure 7. The larger structures ($m \leq 7$) deviate from self-similarity with a peak location biased towards the wall, due to a 'crowding' in the centre region of the pipe. The smaller structures ($m \geq 19$), on the other hand, are limited by $y_\mathrm{p}^+ < 75$, where viscosity becomes important.

The subset of modes for which we expect a self-similar behaviour ($m \in [8, 18]$) is shown in scaled coordinates in figure 8. As previously indicated, the magnitude of each mode is determined such that its l^2-norm is unity, and it has no further meaning. Therefore, each mode is
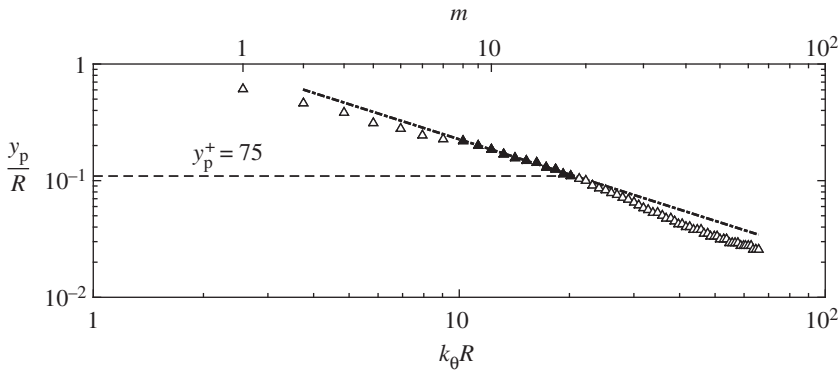
Figure 7. The modal peak locations for the first POD mode ($n = 1$) and azimuthal mode numbers $m \in [1, 64]$. Dash dotted lines, $y_p/R = 2\pi C(k_\theta R)^{-1}$, with $C = 0.36$; dashed lines, peak location $y_p^+ = 75$; filled triangles, region where the mode peaks exhibit a self-similar behaviour ($8 \leq m \leq 18$). The lower abscissa indicates the azimuthal wavenumber, while the upper abscissa indicates the corresponding azimuthal mode number.

re-normalized according to its largest magnitude. The wall normal length scale of the structure may be estimated as either the distance from the wall to its peak location (y_p), or the distance from the peak to the outer edge of the structure where the magnitude of the streamwise component of the first POD mode reaches, say, 5% of its peak value ($y_5 - y_p$). Figure 8a, b shows the streamwise velocity component $\langle \Phi_x^{(n)} \rangle_k$ scaled with the outer radial length scale ($y_5 - y_p$) for the first and second POD modes, respectively. As shown by Hellström *et al.* [31], this scaling yields a promising collapse for the region spanning from the modal peak to the wake region, but not for the near-wall region, indicating that for increasing m the inner radial length scale of the eddies are getting smaller with respect to the outer radial length scale. This feature is further highlighted when the modes are scaled with using the inner radial length scale, suggesting that for the current Reynolds number the largest structures are still influenced by the crowding in the wake region (figure 8c, d). Hence, although there is a range where peak locations exhibit a self-similar behaviour, the modes themselves are not fully self-similar.

The first and second pressure modes, scaled using the outer radial length scale, are shown in figure 8e, f. These modes show a similar collapse to the velocity modes, except for the outer edge of the modes. This non-collapsing behaviour of the pressure mode is more apparent in figure 8g, h, where they are scaled with the inner radial length scale.

The three-dimensionality and evolution of the structures can be visualized using the conditional modes $\Psi^{(n)}(m; \xi, r)$ defined in equation (2.6). The condition for the mode is set at ($\xi/y_p = 0$) and the flow features in the remainder of the domain are set by the flow field itself. The streamwise velocity along with the pressure component of the conditional modes $\Psi^{(1)}(5; \xi, r)$ and $\Psi^{(1)}(10; \xi, r)$ have been chosen as representative structures and are shown in figure 9. Here, the structures are shown in wall-normal units, normalized with y_p. Figure 9a, c shows a coherent structure with a similar behaviour to the LSMs, where the upstream end of the structure is attached to the wall and the downstream end is detached. For this choice of iso-surface, the structures have a streamwise extent of $\mathcal{O}(20y_p)$ at $y/y_p = 1$, for both conditional modes. Although the streamwise extent of the structures depends on the chosen iso-surface, the streamwise repetition of the structures does not. The structures are repeated, with alternating sign, every $\mathcal{O}(20y_p)$; the upstream and downstream structures remain correlated although the correlation level decreases in magnitude. The pressure signatures associated with these low-momentum structures show a low-pressure region in the downstream section of the structure ($\xi/y_p > 0$), spanning from the wall to the full height of the structure, and a high-pressure region in the upstream section of the structure ($\xi/y_p < 0$) spanning the full height of the structure, in good agreement with the observations by Robinson [25].
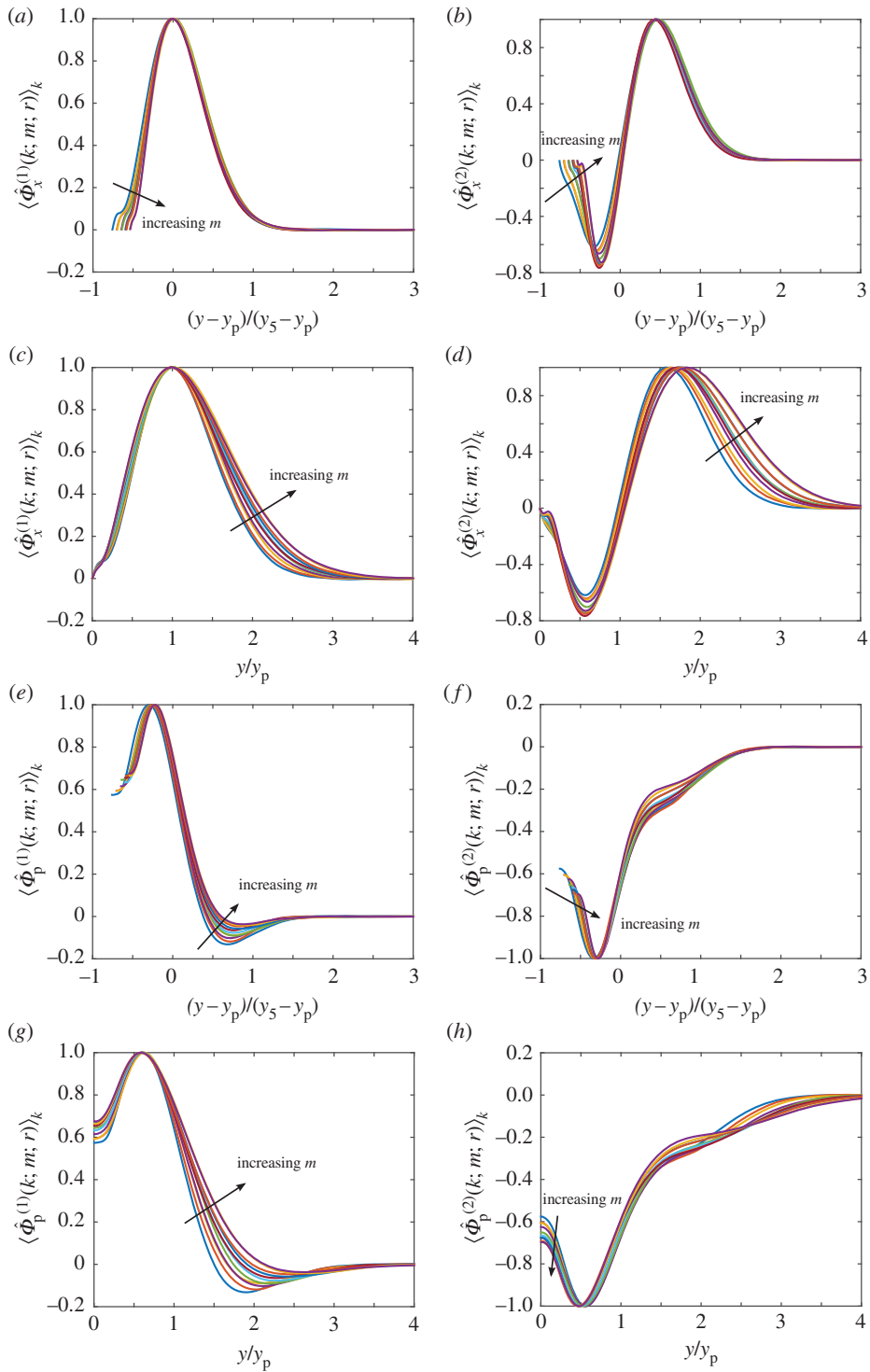
Figure 8. Scaled modes in similarity coordinates proposed by Hellström *et al.* [31]. (*a*, *c*) streamwise component of the first radial mode; (*b*, *d*) streamwise component of the second radial mode; (*e*, *g*) first radial pressure mode; (*f*, *h*) second radial pressure mode. Panels (*a*, *b*, *e*, *f*) are normalized using the outer radial length scale of the first POD mode, while (*c*, *d*, *g*, *h*) are normalized using the inner radial length scale of the first POD mode. All figures are shown for azimuthal modes $m \in [8, 18]$. (Online version in colour.)
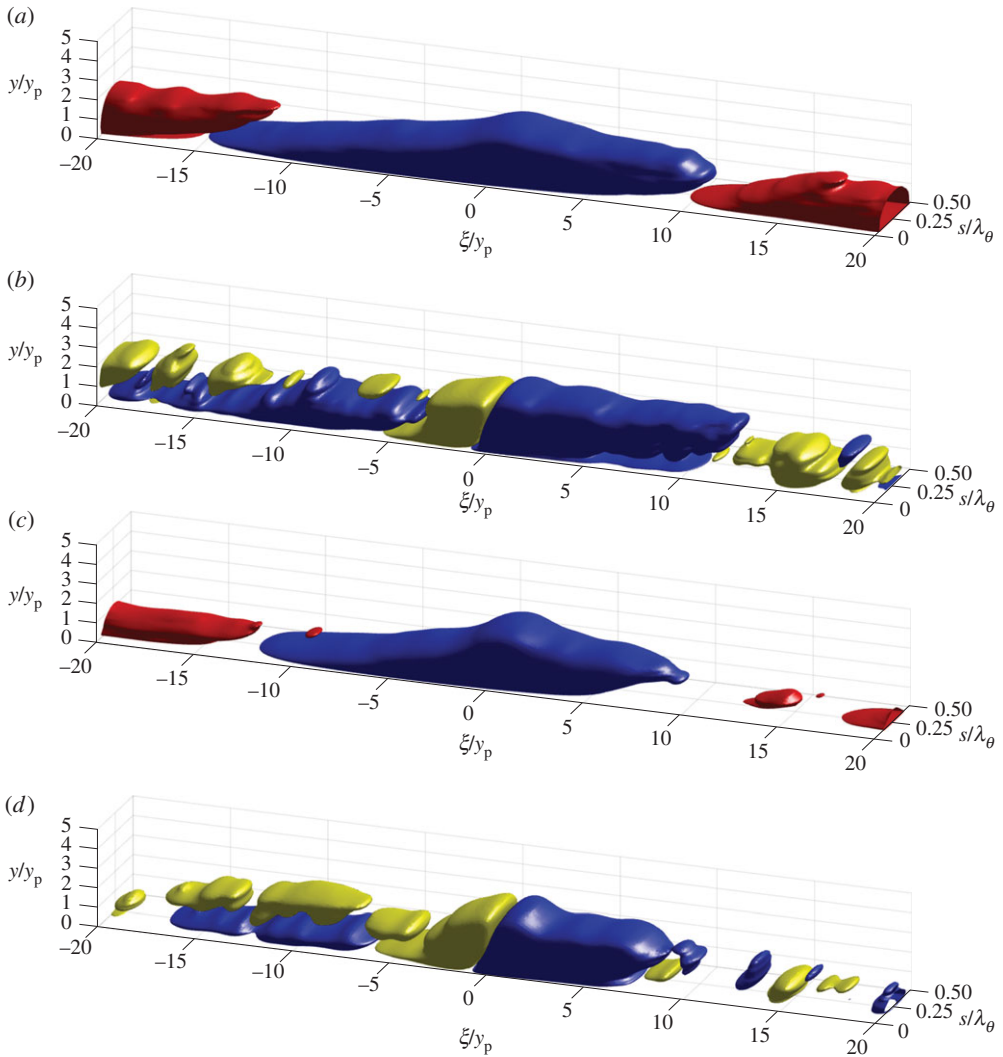
Figure 9. Iso-surfaces of streamwise and pressure components of the conditional mode $\Psi^{(1)}(m; \xi, r)$. (a) Streamwise velocity component for $m = 5$, (b) pressure component for $m = 5$, (c) streamwise velocity component for $m = 10$ and (d) pressure component for $m = 10$. Flow is from left to right. For velocity, red and blue represents positive and negative values, respectively, while for pressure yellow and blue represent positive and negative values, respectively. Iso-surfaces are ±20% the standard deviation of the modes. s/λ_θ represents the scaled azimuthal coordinate.

4. Conclusion

The energetic structures extracted by POD in turbulent pipe flow have previously been shown to give a good representation of the LSMs. Here, we have used the DNS database from Wu *et al.* [34] to investigate the associated pressure field. The POD pressure component was found to be closely linked to the energetic velocity motions, with high- and low-pressure fluctuations corresponding with the core of the LSMs.

The streamwise behaviour and the alignment of the energetic structures were investigated by creating a conditional mode. The condition was set at $\xi/y_P = 0$, while the flow features in the remainder of the domain were determined by the data. These conditional modes showed an alignment of coherent structures independently similar to the LSMs. The structures lined up in the streamwise direction, with a repetition rate of $\mathcal{O}(20y_P)$, and they displayed a low-pressure

field in their downstream section ($\xi/y_\mathrm{p} > 0$), and a high-pressure field in their upstream section ($\xi/y_\mathrm{p} < 0$).

References

1. Kovasznay LSG, Kibens V, Blackwelder RF. 1970 Large-scale motion in the intermittent region of a turbulent boundary layer. *J. Fluid Mech.* **41**, 283–325. (doi:10.1017/S0022112070000629)
2. Murlis J, Tsai HM, Bradshaw P. 1982 The structure of turbulent boundary layers at low Reynolds numbers. *J. Fluid Mech.* **122**, 13–56. (doi:10.1017/S0022112082002080)
3. Kim KC, Adrian RJ. 1999 Very large-scale motion in the outer layer. *Phys. Fluids* **11**, 417–422. (doi:10.1063/1.869889)
4. Weske JR, Plantholt AH. 1953 Discrete vortex systems in the transition range of fully developed flow in a pipe. *J. Aeronaut. Sci.* **10**, 717–718. (doi:10.2514/8.2802)
5. Webb WH, Harrington RP. 1956 Vortex structures in pipe flow. *J. Aeronaut. Sci.* **23**, 792–794. (doi:10.2514/8.3655)
6. Kline SJ, Reynolds WC, Schraub FA, Runstadler PW. 1967 The structure of turbulent boundary layers. *J. Fluid Mech.* **30**, 741–773. (doi:10.1017/S0022112067001740)
7. Head MR, Bandyopadhyay P. 1981 New aspects of turbulent boundary-layer structure. *J. Fluid Mech.* **107**, 297–338. (doi:10.1017/S0022112081001791)
8. Kim J, Moin P, Moser RD. 1987 Turbulence statistics in fully developed channel flow at low Reynolds number. *J. Fluid Mech.* **177**, 133–166. (doi:10.1017/S0022112087000892)
9. Adrian RJ, Meinhart CD, Tomkins CD. 2000 Vortex organization in the outer region of the turbulent boundary layer. *J. Fluid Mech.* **422**, 1–54. (doi:10.1017/S0022112000001580)
10. Wu X, Moin P. 2008 A direct numerical simulation study on the mean velocity characteristics in turbulent pipe flow. *J. Fluid Mech.* **608**, 81–112. (doi:10.1017/S0022112008002085)
11. Lee M, Moser RD. 2015 Direct numerical simulation of turbulent channel flow up to $Re_\tau = 5200$. *J. Fluid Mech.* **774**, 395–415. (doi:10.1017/jfm.2015.268)
12. Berkooz G, Holmes P, Lumley JL. 1993 The proper orthogonal decomposition in the analysis of turbulent flows. *Annu. Rev. Fluid Mech.* **25**, 539–575. (doi:10.1146/annurev.fl.25.010193.002543)
13. Bakewell HP Jr, Lumley JL. 1967 Viscous sublayer and adjacent wall region in turbulent pipe flow. *Phys. Fluids* **10**, 1880–1889. (doi:10.1063/1.1762382)
14. Herzog S, Lumley JL 1978 Determination of large eddy structures in the viscous sublayer: a progress report. In *Proceedings of the dynamic flow conference 1978 on dynamic measurements in unsteady flows*, pp. 869–885. New York, NY: Springer.
15. Aubry N, Holmes P, Lumley JL, Stone E. 1988 The dynamics of coherent structures in the wall region of a turbulent boundary layer. *J. Fluid Mech.* **192**, 115–173. (doi:10.1017/S0022112088001818)
16. Sirovich L, Ball KS, Keefe LR. 1990 Plane waves and structures in turbulent channel flow. *Phys. Fluids A Fluid Dyn.* (*1989–1993*) **2**, 2217–2226. (doi:10.1063/1.857808)
17. Moin P, Moser RD. 1989 Characteristic-eddy decomposition of turbulence in a channel. *J. Fluid Mech.* **200**, 471–509. (doi:10.1017/S0022112089000741)
18. Ball KS, Sirovich L, Keefe LR. 1991 Dynamical eigenfunction decomposition of turbulent channel flow. *Int. J. Numer. Methods Fluids* **12**, 585–604. (doi:10.1002/fld.1650120606)
19. Arroyo MP, Greated CA. 1991 Stereoscopic particle image velocimetry. *Meas. Sci. Technol.* **2**, 1181. (doi:10.1088/0957-0233/2/12/012)
20. Prasad AK, Adrian RJ. 1993 Stereoscopic particle image velocimetry applied to liquid flows. *Exp. Fluids* **15**, 49–60. (doi:10.1007/BF00195595)
21. Del Álamo JC, Jimenez J, Zandonade P, Moser RD. 2006 Self-similar vortex clusters in the turbulent logarithmic region. *J. Fluid Mech.* **561**, 329–358. (doi:10.1017/S0022112006000814)

13

rsta.royalsocietypublishing.org *Phil. Trans. R. Soc. A* **375**: 20160086

22. Sirovich L. 1987 Turbulence and the dynamics of coherent structures. Part 1: Coherent structures. *Quart. Appl. Maths.* **45**, 561–571. (doi:10.1090/qam/910462)
23. Hellström LHO, Smits AJ. 2014 The energetic motions in turbulent pipe flow. *Phys. Fluids* **26**, 125 102– (doi:10.1063/1.4902436)
24. Smits AJ, McKeon BJ, Marusic I. 2011 High-Reynolds number wall turbulence. *Annu. Rev. Fluid Mech.* **43**, 353–375. (doi:10.1146/annurev-fluid-122109-160753)
25. Robinson SK. 1991 The kinematics of turbulent boundary layer structure. *NASA STI/Recon Techn. Rep. N* **91**, 26465.
26. Monty JP, Stewart JA, Williams RC, Chong MS. 2007 Large-scale features in turbulent pipe and channel flows. *J. Fluid Mech.* **589**, 147–156. (doi:10.1017/S002211200700777X)
27. Hellström LHO, Ganapathisubramani B, Smits AJ. 2015 The evolution of large-scale motions in turbulent pipe flow. *J. Fluid Mech.* **779**, 701–715. (doi:10.1017/jfm.2015.418)
28. Hellström LHO, Sinha A, Smits AJ. 2011 Visualizing the very-large-scale motions in turbulent pipe flow. *Phys. Fluids* **23**, 011 703. (doi:10.1063/1.3533016)
29. Bailey SCC, Smits AJ. 2010 Experimental investigation of the structure of large- and very large-scale motions in turbulent pipe flow. *J. Fluid Mech.* **651**, 339–356. (doi:10.1017/S0022112009993983)
30. Baltzer JR, Adrian RJ, Wu X. 2013 Structural organization of large and very large scales in turbulent pipe flow simulation. *J. Fluid Mech.* **720**, 236–279. (doi:10.1017/jfm.2012.642)
31. Hellström LHO, Marusic I, Smits AJ. 2016 Self-similarity of the large-scale motions in turbulent pipe flow. *J. Fluid Mech.* **792**, R1. (doi:10.1017/jfm.2016.100)
32. Hellström LHO, Ganapathisubramani B, Smits AJ. 2016 Coherent structures in transitional pipe flow. *Phys. Rev. Fluids* **1**, 024 403. (doi:10.1103/PhysRevFluids.1.024403)
33. Hwang Y. 2015 Statistical structure of self-sustaining attached eddies in turbulent channel flow. *J. Fluid Mech.* **767**, 254–289. (doi:10.1017/jfm.2015.24)
34. Wu X, Baltzer JR, Adrian RJ. 2012 Direct numerical simulation of a 30R long turbulent pipe flow at $R^+ = 685$: large-and very large-scale motions. *J. Fluid Mech.* **698**, 235–281. (doi:10.1017/jfm.2012.81)
35. McKeon BJ, Sharma AS. 2010 A critical-layer framework for turbulent pipe flow. *J. Fluid Mech.* **658**, 336–382. (doi:10.1017/S002211201000176X)